Characterizing deformability and surface friction of cancer cells

Sangwon Byun[a], Sungmin Son[b], Dario Amodei[c], Nathan Cermak[d], Josephine Shaw[a], Joon Ho Kang[e], Vivian C. Hecht[a], Monte M. Winslow[f,g], Tyler Jacks[f,h], Parag Mallick[c], and Scott R. Manalis[a,b,d,f,1]

Departments of [a]Biological Engineering, [b]Mechanical Engineering, [d]Computational and Systems Biology Initiative, [e]Physics, [h]Biology, and [f]Koch Institute for Integrative Cancer Research, Massachusetts Institute of Technology, Cambridge, MA 02139; and Departments of [c]Radiology and [g]Genetics, Stanford University School of Medicine, Stanford, CA 94305

Edited by David A. Weitz, Harvard University, Cambridge, MA, and approved April 1, 2013 (received for review October 28, 2012)

Metastasis requires the penetration of cancer cells through tight spaces, which is mediated by the physical properties of the cells as well as their interactions with the confined environment. Various microfluidic approaches have been devised to mimic traversal in vitro by measuring the time required for cells to pass through a constriction. Although a cell's passage time is expected to depend on its deformability, measurements from existing approaches are confounded by a cell's size and its frictional properties with the channel wall. Here, we introduce a device that enables the precise measurement of (*i*) the size of a single cell, given by its buoyant mass, (*ii*) the velocity of the cell entering a constricted microchannel (entry velocity), and (*iii*) the velocity of the cell as it transits through the constriction (transit velocity). Changing the deformability of the cell by perturbing its cytoskeleton primarily alters the entry velocity, whereas changing the surface friction by immobilizing positive charges on the constriction's walls primarily alters the transit velocity, indicating that these parameters can give insight into the factors affecting the passage of each cell. When accounting for cell buoyant mass, we find that cells possessing higher metastatic potential exhibit faster entry velocities than cells with lower metastatic potential. We additionally find that some cell types with higher metastatic potential exhibit greater than expected changes in transit velocities, suggesting that not only the increased deformability but reduced friction may be a factor in enabling invasive cancer cells to efficiently squeeze through tight spaces.

cell mechanics | cell stiffness | biophysics | suspended microchannel resonator | biosensors

The ability to quantify the changes that take place during the metastatic process remains a major challenge and is necessary for elucidating the underlying mechanisms as well as for identifying new therapeutic targets. Cellular biomechanics play an important role in metastasis, as cancer cells must not only squeeze through the extracellular matrix and endothelial cell–cell junctions, but they also must travel through small capillaries to reach a distant site. To begin this journey, a cell may undergo an epithelial–mesenchymal transition involving numerous biochemical and cytoskeletal changes that enable it to maintain a motile and invasive state (1–3). As the cell travels and circulates in the bloodstream, its trajectory is influenced by viscoelastic and frictional properties, the latter of which is governed by cell surface interactions as well as normal forces exerted by the cell on the channel wall.

A wide range of approaches for measuring the viscoelastic properties of single cells has been developed and used for addressing this challenge. Techniques such as micropipette aspiration (4, 5), atomic force microscopy (6, 7), and microrheology (8–11) provide highly quantitative and detailed information but have a low throughput. Alternatively, microfluidic approaches (12–20) have led to dramatic increases in throughput but are generally only semiquantitative. Consequently, there has been a general lack of approaches to measure cellular biomechanical properties with both high throughput and high precision. Despite these limitations, two consistent findings have been observed across multiple measurement platforms: (*i*) cancer cells are more deformable than normal cells, and (*ii*) cancer cell deformability correlates with increased metastatic potential (2, 21, 22).

Despite the progress that has been made toward understanding the viscoelastic and frictional properties of single cells in the context of metastasis, the relative significance between the two has been relatively underexplored. Perhaps one of the most straightforward approaches for studying this in vitro is to monitor the movement of a cell as it travels through a fluidic constriction. Such a strategy was initially used to study neutrophil activation (23) and was subsequently adopted for other cell types. In these experiments, deformability was assessed by measuring the total passage time required for the cell to deform into and pass through the constriction. However, there are two obstacles that have made it difficult to delineate the relative contribution of deformability and friction to the total passage time. First, passage time is known to have a power law dependence on cell size (24). Various strategies have been developed for decoupling this dependence. For example, bright-field microscopy has been used to measure cell diameter before entry into the constriction (17), although with limited resolution due to aberrations that can arise from the three-dimensionality of the cell. The Coulter principle has the advantage that it can be implemented without sensitivity to cell shape and orientation, but has the drawback of being difficult to calibrate due to the presence of the constriction (12, 13, 20). Second, in addition to depending on cell size, total passage time lumps together the time required for the cell to squeeze into the constriction, which is primarily dependent on deformability, and the time required to pass through the constriction, which depends on friction with the channel wall. These two regions can be delineated by microscopy (17) but have not yet been observed by the Coulter principle.

To address these obstacles, we have integrated a constriction near the apex of a suspended microchannel resonator (SMR) as shown in Fig. 1*A*. In brief, the SMR consists of a hollow microchannel embedded in a silicon cantilever, whose resonant frequency is detected by the deflection of a laser beam (25). In each experiment, a solution with cells that are denser than the surrounding fluid is flowed into the device. Once a cell enters the SMR, the resonant frequency is lowered by an amount that depends on its buoyant mass and position away from the resonator base (Fig. 1*B*) (25). By tracking the resonant frequency as a cell traverses through the SMR, the position of its center of mass along the channel and its buoyant mass can be measured with a precision near 100 nm and 1 pg, respectively, for a cell that weighs ~100 pg

Author contributions: S.B., S.S., N.C., J.S., J.H.K., V.C.H., M.M.W., T.J., P.M., and S.R.M. designed research; S.B., S.S., N.C., J.S., J.H.K., and V.C.H. performed research; M.M.W. and T.J. contributed mouse model cell lines; S.B., D.A., N.C., and J.S. analyzed data; and S.B., D.A., J.S., P.M., and S.R.M. wrote the paper.

The authors declare no conflict of interest.

This article is a PNAS Direct Submission.

[1]To whom correspondence should be addressed. E-mail: scottm@media.mit.edu.

This article contains supporting information online at www.pnas.org/lookup/suppl/doi:10.1073/pnas.1218806110/-/DCSupplemental.

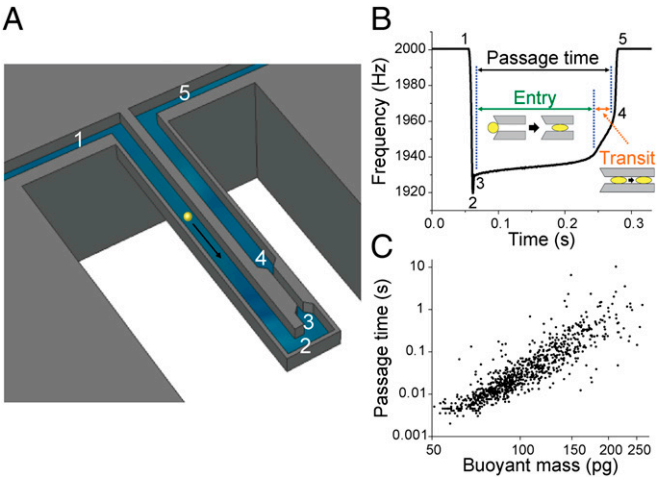

Fig. 1. Schematic diagram of the instrument and data extracted from the measurement. (*A*) Suspended microchannel resonator (SMR) with a constriction (6 μm wide, 15 μm deep, and 50 μm long) located at the apex. A cell passing through an embedded microfluidic channel is deformed as it flows into the constriction. Numbers 1–5 indicate different positions within the microchannel to demonstrate the trajectory of a cell flowing inside the channel. (*B*) The resonant frequency response of the SMR as the cell passes through the microfluidic channel. The numbers 1–5 correspond to the position of the cell in the cantilever, as marked in *A*. The height of the peak corresponds to the buoyant mass of the cell (1 → 2). The cell slows down as it deforms to enter the constriction (entry), and then speeds up as it travels through the constriction (transit). The passage time corresponds to the sum of the entry and transit times (3 → 4). (*C*) Power law dependence of passage time versus buoyant mass for the H1975 cell line (n = 967). Measurements were acquired with a PEG-coated channel surface and using a pressure drop of 1.8 psi.

and travels through the SMR in ∼1 s. As a result, a cell's buoyant mass, passage time, velocity upon entering the constriction (entry velocity), and velocity as it transits through the constriction (transit velocity) can be extracted with a throughput of a few thousand cells per hour. Buoyant mass, which is the metric we use in this study for cell size, is defined by the product of the cell's volume and its density difference from the surrounding fluid.

Using the SMR with the integrated constriction, we demonstrate that precise, single-cell buoyant mass measurements in conjunction with passage time information enable the distinction between cell lines bearing different physical characteristics. More specifically, these combined measurements reveal differences between cell lines arising from blood and epithelial tissue, as well as between cell lines having varying metastatic potential. To assess factors affecting cell passage through the constriction, we further show that entry and transit velocity measurements enable us to identify the relative importance of deformability and surface friction, respectively. Changing the deformability of the cell by perturbing its cytoskeleton primarily alters the entry velocity, whereas changing the surface friction by immobilizing positive charges on the constriction's walls primarily alters the transit velocity. To demonstrate the insight that these parameters provide, we compare the properties of both mouse and human cancer cell lines having known metastatic potentials. When accounting for cell buoyant mass, we find that cells possessing higher metastatic potential exhibit faster entry velocities than cells with lower metastatic potential. However, in some cases, the increase in transit velocities associated with faster entry velocities was considerably greater than expected, suggesting that reduced friction may be a factor in enabling invasive cancer cells to efficiently squeeze through tight spaces. Finally, we demonstrate that combined buoyant mass and passage time measurements can identify tumor cells spiked into blood with a throughput of $\sim 10^5$ cells per h.

Results

Single-Cell Measurement of Buoyant Mass, Passage Time, and Comparison with a Biophysical Model. We first measured the buoyant mass and passage times of hundreds of single cells from a human lung adenocarcinoma cell line, H1975 (Fig. 1*C*), to validate our method. As expected, a cell's passage time through the constriction has a power law relationship to its buoyant mass (24). Interestingly, the range of passage times spans nearly four orders of magnitude as it changes with cell buoyant mass. In addition, the passage time of cells having the same buoyant mass varies by up to an order of magnitude, suggesting the influence of other effects. Compared with other approaches for measuring cell size and passage time through a constriction (12, 13, 17, 20), our results show a thousandfold larger range in passage time across the population and a nearly 10-fold larger variation in passage time for cells of similar buoyant mass. One possible explanation for this discrepancy is that, because the passage times in these previous studies were typically on the millisecond scale and below (12, 20), the relatively higher strain rates diminished the range in the mechanical properties. Although it seems surprising that cells of similar buoyant mass could have such a significant variation in passage time, time lapse microscopy of a cell passing through multiple constrictions in existing literature (26) suggests that, in addition to inherent biological variation, the orientation of the cell upon entry into the constriction could give rise to this spread.

To render our measurement more readily comparable to those obtained via other assays of cell deformability such as micropipette aspiration, we compared the cell trajectories observed in our SMR device to a classical biophysical model of cell entry into a constriction (Fig. 2). We modeled the cell as a homogeneous liquid drop with a viscosity μ_0 that decreases with shear rate according to a power law coefficient b (*SI Materials and Methods*). Our goal in applying it here is to highlight the conceptual similarity between our technique and the classic techniques, not to attempt to derive absolute measures of cell deformability. This "shear-thinning" model has previously been applied to model the aspiration of human neutrophils and other cells into a micropipette (4, 27, 28).

We used the shear-thinning model to predict both the entry times (the time it takes a cell to deform into the constriction; Fig. 1*B*) as well as the trajectories of H1975 cells (n = 343;

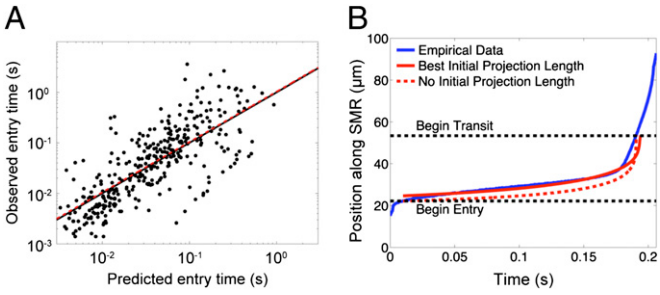

Fig. 2. Trajectories observed in the SMR can be predicted with high accuracy from a power law viscosity model, similar to Tsai et al. (28). (*A*) Prediction of entry times into the constriction for H1975 cells (test set, n = 343). Cells are modeled from a training set (n = 388) as having a shear rate-dependent viscosity $\mu = \mu_0(\gamma)^{-b}$, where a single best-fit model is chosen for all of the cells. The black line shows equality between predicted and observed entry times, the black dots represent individual cells, and the red dashed line is the best fit line for the test set. Predicted entry times and observed entry times demonstrate a high correlation of r = 0.76 in log space. (*B*) Prediction of the detailed trajectory through the constriction using the power law viscosity model, shown for a typical cell with its own best-fit model. The blue line represents the observed trajectory of the cell through the constriction, the dotted red line represents the model prediction, and the solid red line shows the model prediction when an initial projection is incorporated into the model.

SI Materials and Methods). The model's predicted entry times show a strong correlation with the observed entry times (Fig. 2*A*, $r = 0.76$ on a log–log scale). Similarly, strong correlations were obtained for HCC827 (Fig. S1), human lung cancer cell line, which is known to be less invasive than H1975 (29, 30). The shear-thinning model captures the dynamics of entry (Fig. 2*B*) comparably to results obtained on previous platforms. Similar to prior applications of the model, incorporating a small initial projection of the cell into the constriction (28) improves the fit (Fig. S2) (*SI Results*) but does not otherwise significantly alter model parameters. These results suggest that our measurement characterizes the deformation behavior of single cells in a manner akin to those previously achieved by micropipette aspiration.

Then, to determine whether the large span and variance in passage time is exhibited by other types of mammalian cells, we measured seven additional adherent cell lines including mouse embryonic fibroblasts (MEFs), mouse lung cancer cell lines (T_{Met}, T_{nonMet}, and T_{Met}-*Nkx2-1*) (31), human lung cancer cell lines (H1650, H1975, and HCC827), as well as a mouse lymphoblastic leukemia cell line (L1210) that was grown in suspension. Measurements were all acquired with a poly(ethylene glycol) (PEG)-coated channel surface and under a constant applied pressure drop across the microchannel (0.9 psi). All of the measured cell lines exhibited a similar power law dependence between passage time and cell buoyant mass (Fig. 3). However, it is important to note that cell buoyant mass was not the only determining factor of the passage time. As demonstrated by the comparison of the T_{Met} and L1210 cell lines in Fig. 3*C* (Fig. S3), the epithelial lung cancer cells require more time to pass through the constriction than blood cells of similar buoyant mass. From these data, it is clear that neither cell buoyant mass nor passage time alone would be sufficient to distinguish between these two populations of cells. Rather, the combination of the two metrics allows for a clear distinction.

In a similar manner, we found that cell lines with higher metastatic potential exhibit shorter passage times compared with cell lines with lower metastatic potential (Fig. 3 *D–F*). Three pairs of cancer cell lines were compared, and in each pair, one cell line was known to be more metastatic than the other. HCC827 and H1975 are both human lung adenocarcinoma cell lines, but H1975 is more metastatic than HCC827. T_{nonMet} and T_{Met} cell lines were derived from nonmetastatic and metastatic primary mouse lung adenocarcinomas, respectively, with the T_{Met} cell line having greater metastatic ability (31). Down-regulation of the Nkx2-1 transcription factor is a key event in lung cancer metastasis; therefore, T_{Met} cells reexpressing this transcription factor (T_{Met}-*Nkx2-1*) have restricted metastatic potential compared with T_{Met} (31). Hence, the distinction between each pair of cell lines bearing different metastatic potentials is evident when both passage time and buoyant mass information are used together. The difference in passage times was statistically significant for all three pairs (Fig. S4).

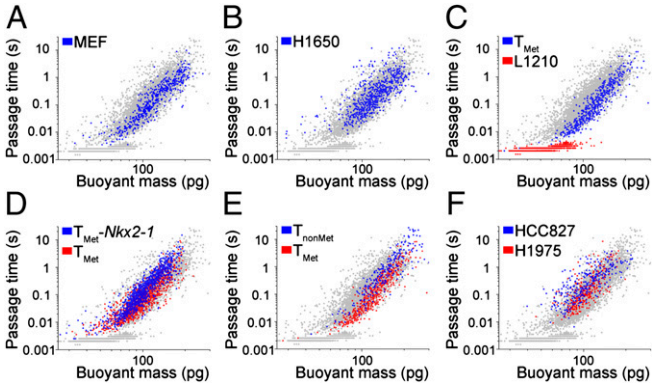

Fig. 3. Power law relationship between passage time and cell buoyant mass is demonstrated by measurements of various cell lines, including (*A*) mouse embryonic fibroblast (MEF) ($n = 511$), (*B*) H1650 ($n = 639$), (*C*) T_{Met} (blue, $n = 512$), L1210 (red, $n = 1401$), (*D*) T_{Met}-*Nkx2-1* (blue, $n = 1065$), T_{Met} (red, $n = 1028$), (*E*) T_{nonMet} (blue, $n = 252$), T_{Met} (red, same dataset as in *C*), (*F*) HCC827 (blue, $n = 278$), and H1975 (red, $n = 307$). Measurements were made in a PEG-coated channel under a constant pressure drop of 0.9 psi. The gray dots shown as a background correspond to the collection of all measured cell lines. Notably, as shown in *C*, adherent mouse lung cancer cells in suspension require a longer time to pass through the constriction than mouse blood cells of similar buoyant mass. Three pairs of cancer cell lines having different known metastatic potentials are compared in *D–F*. In each pair, the cell line with the higher metastatic potential (red dots) exhibits shorter passage times than those with the lower metastatic potential (blue dots). The difference in passage time was statistically significant for all three pairs in *D–F* (Fig. S4).

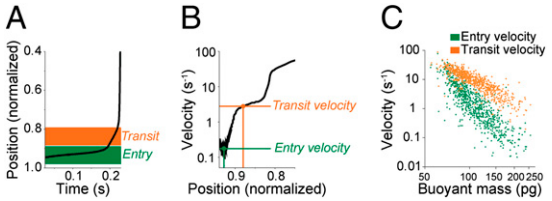

Fig. 4. Extracting entry and transit velocities from single cell measurement. (*A*) The resonant frequency response (positions 3–5 in Fig. 1*B*) is converted to the normalized position of the cell in the cantilever and plotted versus time. The length of the cantilever was normalized to 1 to represent the cell's position, where 1 and 0 correspond to the tip and base, respectively. (*B*) Cell velocity is obtained by taking the time derivative of the normalized position. Entry and transit velocities are extracted at specific locations that correspond to the entrance and the inside of the constriction, respectively. (*C*) Entry (green) and transit (orange) velocities versus buoyant mass for the data set from Fig. 1*C*.

Entry and Transit Velocities Reveal the Relative Significance Between Deformability and Surface Friction. To assess the components that govern passage time, the entry and transit velocities were extracted from the SMR measurements. The passage of each cell through the constricted microchannel comprises the initial deformation of the cell to enter the constriction as well as the subsequent transit of the cell through the constriction. The velocity of each cell during its entry and transit can be obtained by monitoring the position of its center of mass within the microchannel (Fig. 4 *A* and *B*), as given by the resonant frequency shift of the cantilever (32). Both entry and transit velocities have a power law dependence on the buoyant mass, similar to the passage time, but the velocities decrease with increasing buoyant mass (Fig. 4*C*). Also, for a given cell, the entry velocity is slower than the transit velocity. However, the difference between the entry and transit velocities is less pronounced for smaller cells, because smaller cells require less time to deform into the constriction in comparison with larger cells. Hence, in complement with passage time information, the entry and transit velocities can provide more insight into cellular properties governing the passage through the constriction.

Next, the effects of deformability and surface friction on the passage of cells through the constriction were assessed by measuring H1975 cells under two separate conditions—having perturbed its cytoskeleton with latrunculin B (LatB), and having coated the microchannel surface with positively charged poly-L-lysine (PLL) (Fig. 5). First, as expected, the treatment with LatB decreased the passage time of the cells (Fig. S5*A*), corresponding to the LatB-induced increase in cell deformability by the disruption of actin filaments (33). Furthermore, the LatB treatment increased both entry and transit velocities, with the relative increase in entry velocity being greater than that of transit velocity

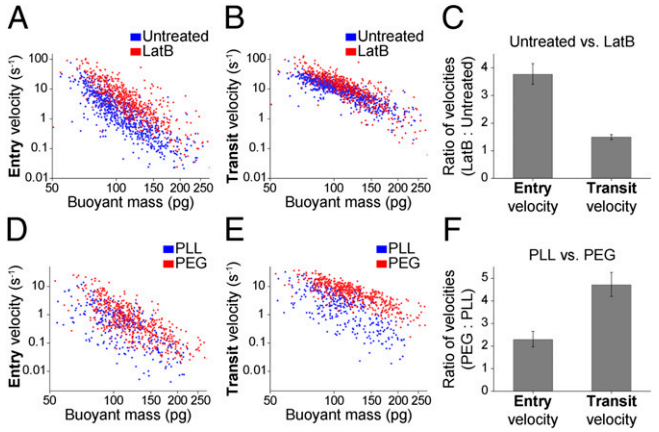

Fig. 5. Changes in the entry and transit velocities of H1975 cells after perturbing either deformability or microchannel surface charge. (*A*) Entry velocity and (*B*) transit velocity versus buoyant mass for H1975 untreated (blue, $n = 843$) and treated with LatB (red, $n = 907$, 5 μg/mL for 30 min) measured in a PEG-coated channel. Treatment with LatB decreases the passage time of H1975 (Fig. S5) and induces a larger shift in entry velocity than transit velocity. (*C*) A ratio of velocities from the two conditions was calculated as in Fig. S12. Changing the deformability of the cell by perturbing its actin cytoskeleton induces a 3.8-fold increase in the entry velocity, and only a 1.5-fold increase in the transit velocity. (*D*) Entry velocity and (*E*) transit velocity versus buoyant mass for H1975 cells passing through a microchannel whose surface is coated with positively charged PLL (blue, $n = 345$) or neutral PEG (red, $n = 649$). PLL increases the passage time (Fig. S5) and results in a greater shift in transit velocity than entry velocity. (*F*) Changing the surface friction from PEG to PLL caused entry velocity to decrease 2.3-fold, and transit velocity to decrease 4.7-fold. Error bars represent 95% confidence intervals. All measurements were acquired using a pressure drop of 1.8 psi.

(Fig. 5 *A*–*C*). Although the small change in transit velocity indicates that a change in cell stiffness can influence the friction because the normal force of the cell against the channel wall is altered (34), the greater change in entry velocity is consistent with the fact that perturbing the viscoelastic properties of the cell affects the passage most when the deformation of the cell is critical, i.e., at the entry rather than during transit. A similar behavior was observed when MEF cells were treated with nocodazole (Fig. S6), further demonstrating that a cytoskeletal deformability change in the cell corresponds to a larger shift in entry velocity than transit velocity.

Coating the microchannel constriction with PLL increased the passage time of the cells (Fig. S5*B*), corresponding to the increased interaction of the negatively charged cell surface with the positively charged PLL-coated channel surface than with the neutral PLL-graft-PEG–coated surface. The PLL coating decreased both the entry and transit velocities, but with a larger change in transit velocity (Fig. 5 *D*–*F*). Although the surface interaction during the deformation at the constriction entry was nontrivial, the effect was greatest when the contact area between the cell and the channel wall was maximum, i.e., during the cell's transit through the constriction. The transit velocity thus represents a friction measurement that encapsulates effects contributing to the normal force exerted by the cell on the channel wall, as well as interactions between the surface of the cell and the channel. The experiment involving a PLL surface coating demonstrates that enhancing surface interactions, such as those governed by charge, alters the transit velocity more than entry velocity. Similar results were obtained for various other cell lines, such as HCC827, T_{Met}, and T_{nonMet} (Fig. S7). Hence, even though deformability and friction are not completely orthogonal in our measurements, the relative differences in entry and transit velocities provide a metric for the relative importance of deformability and friction during the passage of a cell through a constriction.

Characterizing Entry and Transit Velocities of Cancer Cells Reveals That Deformability and Friction Govern Cell Passage Time. We also found that the relative importance of the cell's deformability and surface friction to its passage through the constriction could be a unique indicator of cell state. The deformation and friction properties of cancer cells having different known metastatic potentials were characterized by entry and transit velocities on a PEG-coated channel (Fig. 6). In addition to having shorter passage times (Fig. 3 *D*–*F*), all three cell lines with higher metastatic potential exhibit faster entry and transit velocities. Interestingly, the relative differences in entry and transit velocities from each pair showed distinct patterns. Expressing the Nkx2-1 transcription factor in T_{Met} led to a change primarily in entry velocity, which is similar to what we observed in altering the cytoskeletal deformability of the cells with LatB (Fig. 5*C*). In contrast, T_{Met} versus T_{nonMet} showed significant differences in both entry and transit velocities, suggesting that changes in friction account for more of the difference between this pair of cells than between the pair with a single genetic alteration (T_{Met} versus T_{Met}-*Nkx2-1*). H1975 versus HCC827 also demonstrated that a considerable change in the transit velocity is associated with the entry velocity. These examples suggest that reduced friction may play a role in enabling invasive cancer cells to effectively squeeze through tight spaces. It is possible that such changes in friction may be related to differences in factors contributing to the normal force of the cell on the channel wall, such as cell relaxation times. Additionally, the observed changes may be caused by glycocalyx characteristics, such as the expression of particular cell surface molecules like sialic acid, because it is already known that increased expression of sialic acid may be accompanied with a higher metastatic potential in cancer cells (35).

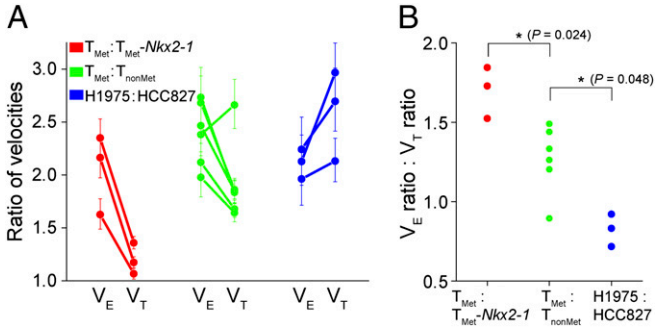

Fig. 6. Three pairs of cancer cell lines having different metastatic potentials (T_{Met} versus T_{Met}-*Nkx2-1*, red; T_{Met} versus T_{nonMet}, green; and H1975 versus HCC827, blue) were compared by measuring the changes in entry velocity (V_E) and transit velocity (V_T) with a PEG-coated channel surface. (*A*) Ratio of V_E and ratio of V_T for three pairs of cancer cell lines. V_E and V_T ratios connected by a line represent one replicate. In contrast to T_{Met} versus T_{Met}-*Nkx2-1*, T_{Met} versus T_{nonMet} and H1975 versus HCC827 show that a significant change in transit velocity is associated with a change in entry velocity, suggesting that the role of friction is more significant in those pairs. T_{Met} versus T_{Met}-*Nkx2-1*, T_{Met} versus T_{nonMet}, and H1975 versus HCC827 were repeated from different cultures three, six, and three times, respectively. Error bars represent 95% confidence intervals. (*B*) For each measurement, the ratio of V_E divided by the ratio of V_T is shown, which confirms that the proportional change in V_E relative to V_T was significantly different among the three pairs (*$P < 0.05$, Mann–Whitney–Wilcoxon test). Measurements were acquired using a pressure drop of 0.9 psi for the mouse cell lines (T_{Met}, T_{Met}-*Nkx2-1*, T_{nonMet}) and a higher drop of 1.8 psi for the human cell lines (H1975, HCC827) to account for their larger size.

Effects of Cell Density on SMR Measurements. As a cell's buoyant mass depends on its volume and difference in its density with the surrounding fluid, we sought to identify effects of cell density on the trends found in the deformability and friction measurements made by the SMR. We measured the average density of each cell line (*SI Materials and Methods*) and thus converted the buoyant mass to volume (Fig. S8) (*SI Results*) (36). Passage times, entry velocities, and transit velocities of cancer cells with varying metastatic potentials (Figs. 3 *D–F* and 6) were compared again based on cell volume (Figs. S8 and S9). Interestingly, we found that the difference in density between human lung cancer cell lines was more significant than that between mouse lung cancer cell lines. Because HCC827 cells had a significantly lower density than H1975 cells, passage time properties for these two cell lines, when plotted versus cell volume, were similar. In contrast, the density of mouse lung cancer cell lines (i.e., T_{Met} versus T_{Met}-*Nkx2-1* and T_{Met} versus T_{nonMet}) was only slightly different, and therefore the passage time properties of those cell lines remained similar when plotted versus the volume. Thus, differences between passage time properties for all three cell line pairs were consistent with expected deformability changes based on metastatic potential when accounting for buoyant mass, but not when accounting for volume. Furthermore, the differences in cell density did not change the findings from characterizing entry and transit velocities shown in Fig. 6 (Fig. S9). Density measurements in combination with deformability and friction measurements may shed light on further interesting characteristics of cancer cells, which can be studied more in depth in future work.

Using SMR Measurements to Discriminate Between Human Epithelial and Blood Cells. As an application of using passage time measurements of single cells in the SMR, we demonstrate the ability of the SMR to discriminate between cells arising from human blood versus epithelium. A human buffy coat sample was spiked with H1650 cells, and the buoyant mass and passage time of each cell was recorded. Fig. 7 portrays that blood cells transit through the constriction several orders of magnitude faster than spiked H1650 cells, and that the SMR signals generated by the two types of cells are quite distinct. Hence, in general, H1650 cells can be distinguished from blood cells based on the passage time and buoyant mass measurements. Among the total of $\sim 10^4$ cells counted in the spiked sample, the number of cells having a long passage time (greater than 8 ms) was 103, which closely corresponds to the expected value from the spiked concentration of H1650 cells (~1:90). Thus, the SMR platform may provide a tool to distinguish circulating tumor cells (CTCs) from the surrounding blood cells, irrespective of molecular surface expression (37, 38). Moreover, the throughput of the SMR is $\sim 10^5$ cells per h ($\sim 10^4$ cells detected for 6 min), which is sufficient for interrogating patient samples provided upstream enrichment strategies are used (e.g., CD45 depletion) (39, 40). Therefore, in the future it may be feasible to use the SMR with constriction to identify CTCs in patient blood samples based on biophysical properties, which may reveal populations of CTCs that have gone undetected by common methods involving specific molecular probes. In addition, parsing out transit and entry velocity information could increase our understanding of the biophysical characteristics of CTCs. As the cells remain viable and proliferate well after measurement in the SMR (Fig. S10), we could later perform downstream molecular and functional analyses on identified CTCs.

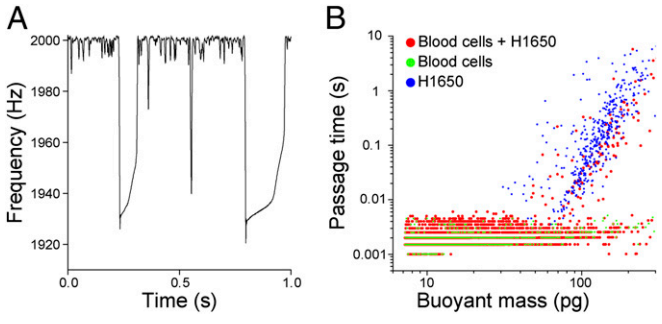

Fig. 7. Passage time versus buoyant mass measurements delineate H1650 cells from human blood cells. (*A*) Peaks detected from the blood cells spiked with H1650 cells, where each peak represents the transit of a cell through the SMR. (*B*) Passage time versus buoyant mass for H1650 and blood cells. Blood cells (green, $n = 2832$) traveled through the constriction several orders of magnitude faster than H1650 cells (blue, $n = 404$), suggesting that H1650 cells could be distinguished from blood cell populations by passage time. Indeed, the spiked sample (red, $n = 10810$) shows a subpopulation whose passage time and buoyant mass match that of the H1650 cells. Measurements were acquired with a PEG-coated channel surface and using a pressure drop of 1.5 psi.

Conclusion

The SMR can precisely weigh individual cells and measure their position along the channel with high spatial resolution. We have used this capability along with an integrated constriction in the microchannel, first to decouple cell size from passage time information, as a measure of holistic cellular deformability. More excitingly, the SMR further enables us to track a cell's velocity as it flows through the constriction and infer the relative significance between deformability and surface friction of cancer cells. Indeed, we have shown that deformability and friction characteristics can be linked to even a single genetic alteration known to govern metastatic potential in cancer cells. Our results suggest that there may be genetic alterations that preferentially modulate friction and that these could be possible drivers for metastatic potential. In addition, we have demonstrated a preliminary study that establishes the feasibility of using the SMR system to identify and study CTCs. This approach has the particular advantage of not relying upon specific molecular markers, which may bias the selection of CTCs. Thus, measurements of single-cell buoyant mass, deformability, and friction may help to elucidate biophysical properties of cancer cells in circulation and in relation to processes involved in metastasis.

Materials and Methods

Experimental System. As described by Burg et al. (25), cells suspended in solution flow through the SMR, and the resulting frequency shift depends on the buoyant mass and position of the cell. SMR devices with a constriction were fabricated by creating buried channels in silicon-on-insulator wafers, followed by wafer thinning and dry etching to form suspended microchannels with 2- to 3-μm thin walls and a 15-μm channel depth. Two hundred devices are fabricated and vacuum-packaged on a 6-inch wafer with yields exceeding 80%. A getter layer prevents slow degradation of the on-chip vacuum due to outgassing. Integrated under each cantilever is an electrostatic drive electrode and the cantilever vibration is detected by the optical lever. A gain controlled oscillator circuit is used to continuously track the resonant frequency of the SMR device. Although we can observe each cell as it enters the SMR, the constraints of our device make it impractical to obtain a precise measure of cell volume with our microscope. It is also important to note that to track the position of the cell as it travels through the constriction, we monitor the resonant frequency of the cantilever, which can achieve a precision near 100 nm for cell velocities of ~0.5 mm/s. The position of the cell cannot be tracked by microscopy because the walls of the suspended channel are not transparent. The length of the cantilever is 316 μm with the rectangular microchannel of 20 μm wide and 15 μm deep. The constriction located near the apex of the microchannel is 50 μm long and the width of cross-section is 6 μm. Cells enter and exit the SMR through two on-chip bypass channels that flank the SMR (Fig. S11). Fluid flow through the bypass channels is controlled by two electronic pressure regulators and three solenoid valves. Cells are introduced through the inlet of the bypass channel, whereas the other three outlets are filled with cell culture medium. A constant pressure drop is maintained across the fluidic channels by the pressure regulators that drive the cells through the SMR (Fig. S11).

Channel Wall Coating. The fluidic channel of the device was coated with PEG [1 mg/mL; PLL(20)-g[3.5]-PEG(2); Surface Technology] or PLL (0.1 mg/mL; R&D Systems) before all experiments. All results from Figs. 1–4, 5 *A*–*C*, 6, and 7 were measured with PEG-coated surface. In Fig. 5 *D*–*F*, the results from PLL-coated surface was compared with those from PEG-coated surface. Before the coating, the channel was cleaned with piranha solution (3:1 mixture of H_2SO_4 and H_2O_2) for 15 min at room temperature, followed by a thorough rinse with deionized H_2O (dH_2O). The channel was briefly dried with air before adding PEG or PLL solution. For a PEG coating, a slow flow of PEG was kept in the SMR for 1 h. The channels were then dried with air and rinsed with dH_2O. For a PLL coating, PLL was maintained in the SMR for 2 h, followed by drying with air and rinsing with PBS and dH_2O.

Cell Preparation. All cell lines, including MEF (33), T_{Met}, T_{Met}-*Nkx2-1*, T_{nonMet} (31), H1650, H1975, HCC827 (29, 30), and L1210 (41), were cultured under standard conditions as described elsewhere. Materials used for cell culture are listed in Table S1 for each cell line. The T_{nonMet} cell line (368T1) and T_{Met} cell line (393T5) were generated from tumors that developed in *Kras*$^{LSL\text{-}G12D}$; *p53*^{floxflox} mice after intratracheal lentiviral-Cre infection (31). T_{Met}-*Nkx2-1* cells were generated through retroviral expression of Nkx2-1 in a T_{Met} cell line (389T2) (31). T_{nonMet} cells (368T1) were compared with T_{Met} cells (393T5). T_{Met}-*Nkx2-1* cells were compared with its control T_{Met} cells (389T2). Cells were passaged 1 or 2 d before the experiment. To harvest the cells, the culture medium was aspirated, cells were rinsed with PBS, and trypsin was used to detach the adherent cell types from the flask. Cells were then aspirated and resuspended in culture media to a concentration of 0.5–1 $\times$ 10^6 cells per mL The cell solution was filtered through a 30-μm mesh (Miltenyi Biotec) before measurement in the SMR. To treat the cells with LatB, the cells were dissociated from the surface, resuspended in the medium with 5 μg/mL LatB, and kept in the 37 °C incubator for 30 min before loading the cells in the SMR device. To maintain the LatB-treated condition during the experiment, the medium used in the SMR device was also supplemented with LatB. Treating the cells with LatB in a suspended state for up to 1 h did not alter the viability and proliferation rate when they were replated on a flask after replacing the medium with normal growth medium.

Spiked Cells Experiment. To test whether the SMR can identify tumor cells among a heterogeneous population of cells, human blood cells were spiked with a known concentration of human lung cancer cells, H1650. Human blood cells were prepared from buffy coat (Research Blood Components). First, red blood cells in the buffy coat were removed by Histopaque-1077 (Sigma-Aldrich). Briefly, 3 mL of buffy coat was overlaid onto an equal volume of Histopaque solution. It was centrifuged at 821 $\times$ *g* for 15 min at room temperature. The center layer containing nucleated cells was then carefully extracted using a pipette and resuspended in PBS (821 $\times$ *g*, 10 min). This was diluted to a final concentration of ~8 $\times$ 10^6 cells per mL, which was measured by a Coulter counter (Multisizer 4; Beckman Coulter). Then, ~9 $\times$ 10^4 cells per mL H1650 cells was spiked into the blood cells. Although CTC cells are much rarer in patient samples, the higher concentration of spiked cells enabled us to acquire enough data in a given time to demonstrate that tumor cells can be distinguished from blood cells using our instrument. The passage time for blood cells, H1650, and a mixture of blood cells and H1650 cells were separately measured under the same conditions, using a pressure drop of 1.5 psi. The resulting flow rate was 38 μL/h as measured with blank media.

Data Processing. Buoyant mass, passage time, entry velocity, and transit velocity information were obtained by processing the resonant frequency data from the SMR. Details are included in *SI Materials and Methods*.

ACKNOWLEDGMENTS. We thank D. Wirtz (The Johns Hopkins University) for valuable discussions and the MEF cell line. We acknowledge support from the National Cancer Institute Contracts CCNE-T (Grant 26697290-47281-A) and Physical Sciences Oncology Center U54CA143874 as well as from Stand Up to Cancer (SU2C/AACR).

1. Kalluri R, Weinberg RA (2009) The basics of epithelial-mesenchymal transition. *J Clin Invest* 119(6):1420–1428.
2. Wirtz D, Konstantopoulos K, Searson PC (2011) The physics of cancer: The role of physical interactions and mechanical forces in metastasis. *Nat Rev Cancer* 11(7):512–522.
3. Kumar S, Weaver VM (2009) Mechanics, malignancy, and metastasis: The force journey of a tumor cell. *Cancer Metastasis Rev* 28(1–2):113–127.
4. Drury JL, Dembo M (2001) Aspiration of human neutrophils: Effects of shear thinning and cortical dissipation. *Biophys J* 81(6):3166–3177.
5. Hochmuth RM (2000) Micropipette aspiration of living cells. *J Biomech* 33(1):15–22.
6. Hansma HG, Hoh JH (1994) Biomolecular imaging with the atomic force microscope. *Annu Rev Biophys Biomol Struct* 23:115–139.
7. Radmacher M (2002) Measuring the elastic properties of living cells by the atomic force microscope. *Methods Cell Biol* 68:67–90.
8. Bausch AR, Ziemann F, Boulbitch AA, Jacobson K, Sackmann E (1998) Local measurements of viscoelastic parameters of adherent cell surfaces by magnetic bead microrheometry. *Biophys J* 75(4):2038–2049.
9. Tseng Y, Kole TP, Wirtz D (2002) Micromechanical mapping of live cells by multiple-particle-tracking microrheology. *Biophys J* 83(6):3162–3176.
10. Wang N, Butler JP, Ingber DE (1993) Mechanotransduction across the cell surface and through the cytoskeleton. *Science* 260(5111):1124–1127.
11. Yamada S, Wirtz D, Kuo SC (2000) Mechanics of living cells measured by laser tracking microrheology. *Biophys J* 78(4):1736–1747.
12. Adamo A, et al. (2012) Microfluidics-based assessment of cell deformability. *Anal Chem* 84(15):6438–6443.
13. Chen J, et al. (2011) Classification of cell types using a microfluidic device for mechanical and electrical measurement on single cells. *Lab Chip* 11(18):3174–3181.
14. Gossett DR, et al. (2012) Hydrodynamic stretching of single cells for large population mechanical phenotyping. *Proc Natl Acad Sci USA* 109(20):7630–7635.
15. Guck J, et al. (2001) The optical stretcher: A novel laser tool to micromanipulate cells. *Biophys J* 81(2):767–784.
16. Hirose Y, et al. (2010) A new stiffness evaluation toward high speed cell sorter. *2010 IEEE International Conference on Robotics and Automation* (IEEE, Piscataway, NJ), pp 4113–4118.
17. Hou HW, et al. (2009) Deformability study of breast cancer cells using microfluidics. *Biomed Microdevices* 11(3):557–564.
18. Hur SC, Henderson-MacLennan NK, McCabe ERB, Di Carlo D (2011) Deformability-based cell classification and enrichment using inertial microfluidics. *Lab Chip* 11(5):912–920.
19. Rosenbluth MJ, Lam WA, Fletcher DA (2008) Analyzing cell mechanics in hematologic diseases with microfluidic biophysical flow cytometry. *Lab Chip* 8(7):1062–1070.
20. Zheng Y, Shojaei-Baghini E, Azad A, Wang C, Sun Y (2012) High-throughput biophysical measurement of human red blood cells. *Lab Chip* 12(14):2560–2567.
21. Swaminathan V, et al. (2011) Mechanical stiffness grades metastatic potential in patient tumor cells and in cancer cell lines. *Cancer Res* 71(15):5075–5080.
22. Xu W, et al. (2012) Cell stiffness is a biomarker of the metastatic potential of ovarian cancer cells. *PLoS One* 7(10):e46609.
23. Pécsvárady Z, Fisher TC, Fabók A, Coates TD, Meiselman HJ (1992) Kinetics of granulocyte deformability following exposure to chemotactic stimuli. *Blood Cells* 18(2): 333–352, discussion 353–358.
24. Bathe M, Shirai A, Doerschuk CM, Kamm RD (2002) Neutrophil transit times through pulmonary capillaries: The effects of capillary geometry and fMLP-stimulation. *Biophys J* 83(4):1917–1933.
25. Burg TP, et al. (2007) Weighing of biomolecules, single cells and single nanoparticles in fluid. *Nature* 446(7139):1066–1069.
26. Gabriele S, Versaevel M, Preira P, Théodoly O (2010) A simple microfluidic method to select, isolate, and manipulate single-cells in mechanical and biochemical assays. *Lab Chip* 10(11):1459–1467.
27. Lim CT, Zhou EH, Quek ST (2006) Mechanical models for living cells—a review. *J Biomech* 39(2):195–216.
28. Tsai MA, Frank RS, Waugh RE (1993) Passive mechanical behavior of human neutrophils: Power-law fluid. *Biophys J* 65(5):2078–2088.
29. Yauch RL, et al. (2005) Epithelial versus mesenchymal phenotype determines in vitro sensitivity and predicts clinical activity of erlotinib in lung cancer patients. *Clin Cancer Res* 11(24 Pt 1):8686–8698.
30. Walter K, et al. (2012) DNA methylation profiling defines clinically relevant biological subsets of non-small cell lung cancer. *Clin Cancer Res* 18(8):2360–2373.
31. Winslow MM, et al. (2011) Suppression of lung adenocarcinoma progression by Nkx2-1. *Nature* 473(7345):101–104.
32. Dohn S, Svendsen W, Boisen A, Hansen O (2007) Mass and position determination of attached particles on cantilever based mass sensors. *Rev Sci Instrum* 78(10):103303.
33. Lee JS, et al. (2007) Nuclear lamin A/C deficiency induces defects in cell mechanics, polarization, and migration. *Biophys J* 93(7):2542–2552.
34. Gabriele S, Benoliel AM, Bongrand P, Théodoly O (2009) Microfluidic investigation reveals distinct roles for actin cytoskeleton and myosin II activity in capillary leukocyte trafficking. *Biophys J* 96(10):4308–4318.
35. Yogeeswaran G, Salk PL (1981) Metastatic potential is positively correlated with cell surface sialylation of cultured murine tumor cell lines. *Science* 212(4502):1514–1516.
36. Bryan AK, Goranov A, Amon A, Manalis SR (2010) Measurement of mass, density, and volume during the cell cycle of yeast. *Proc Natl Acad Sci USA* 107(3):999–1004.
37. Nagrath S, et al. (2007) Isolation of rare circulating tumour cells in cancer patients by microchip technology. *Nature* 450(7173):1235–1239.
38. Stott SL, et al. (2010) Isolation of circulating tumor cells using a microvortex-generating herringbone-chip. *Proc Natl Acad Sci USA* 107(43):18392–18397.
39. Yang L, et al. (2009) Optimization of an enrichment process for circulating tumor cells from the blood of head and neck cancer patients through depletion of normal cells. *Biotechnol Bioeng* 102(2):521–534.
40. Liu Z, et al. (2011) Negative enrichment by immunomagnetic nanobeads for unbiased characterization of circulating tumor cells from peripheral blood of cancer patients. *J Transl Med* 9:70.
41. Son S, et al. (2012) Direct observation of mammalian cell growth and size regulation. *Nat Methods* 9(9):910–912.

Supporting Information

Byun et al. 10.1073/pnas.1218806110

SI Results

Biophysical Model—Population Results. As discussed in *SI Materials and Methods*, we used the shear-thinning model to predict the entry times into the constriction of a large set of H1975 and HCC827 human lung cancer cells as well as murine T_{Met}, T_{nonMet}, and T_{Met}-*Nkx2-1* cells. Parameters were derived from training sets of cells and then applied to test sets. Our goal in applying the shear thinning was to highlight the conceptual similarity between our technique and the classic techniques, like micropipette aspiration, rather than to attempt to extract absolute measures of cell deformability. For this population level version of the model (*SI Materials and Methods*), we estimated a single set of model parameters for the each cell type. We compared the entry times predicted by the model with those observed in the cell trajectory data. Fig. S1 *A* and *B* show graphs of log(predicted entry times) against log(observed entry times), for the H1975 and HCC827 datasets, respectively. The log(predicted entry times) and log(observed entry times) demonstrated a strong linear trend, with correlations $r = 0.76$ and $r = 0.74$ for H1975 and HCC827, respectively. Fits for T_{Met}, T_{nonMet}, and T_{Met}-*Nkx2-1* cell lines had correlations of 0.89, 0.87, and 0.92, respectively.

Biophysical Model—Single-Cell Results. In addition to testing the shear-thinning model on the entire populations of cells, we also tested the model on individual cells. As described in *SI Materials and Methods*, we allowed each cell to have its own viscosity dependence parameter b, while still fixing the parameter μ_0 across the population. This allowed us to exactly match the model's predicted entry time for each cell to the observed entry time, while preserving the detailed shape of the trajectory as an independent test of the model's quality. Some typical cell trajectory fits are shown in Fig. S2*A*, particularly highlighting the best, 25th percentile, median, and 75th percentile quality fits for the H1975 dataset, where the quality of fit is measured by the model error score (*SI Materials and Methods*).

Overall, it is clear that some cells fit the model extremely well (Fig. S2*A*, *Upper Left*), whereas others fit it poorly (*Lower Right*). In general, cells with a long entry time tend to fit the model better than cells with a short entry time. We believe that the discrepancy at short entry times may be due to the fact that the shear-thinning model does not take into account the transit time or friction, which we have shown to be important at short entry times. Thus, it is possible that a more sophisticated model may improve the fit results.

The model fit is shown both with and without an initial projection (*SI Materials and Methods*). The initial projection substantially improves the quality of many fits, as confirmed by a box-and-whiskers plot of mean squared error for both the H1975 cells and the HCC827 cells (Fig. S2*B*). This improvement is seen both on average and for most individual cells. The optimal initial projection length is clustered around 1% of the cantilever length, corresponding to a 3-μm-long initial insertion of the cell into the constriction.

Density of Cancer Cells with Varying Metastatic Potentials. Density measurements of three pairs of cancer cell lines are shown in Fig. S8. The density of mouse lung cancer cell lines, T_{Met} (389T2) versus T_{Met}-*Nkx2-1* (derived from 389T2) and T_{Met} (393T5) versus T_{nonMet} (368T1), was only slightly different (Fig. S8*A*). The less metastatic T_{Met}-*Nkx2-1* cells have a slightly higher density (1.0515 ± 0.0008 g/mL, mean ± SD) compared with the more metastatic T_{Met} cells (1.0506 ± 0.0010 g/mL). As a result, the passage time difference between the two cell lines is slightly more pronounced when plotted versus the volume (Fig. S8*B*). Next, the less metastatic T_{nonMet} cells have only a slightly lower density (1.0528 ± 0.0017 g/mL) than the more metastatic T_{Met} cells (1.0537 ± 0.0022 g/mL). In this case, the passage time properties of those cell lines remained similarly distinguishable when plotted versus cell volume as with buoyant mass (Fig. S8*C*). In the case of the human EGFR mutant lung cancer cell lines, the cells with lower metastatic potential (HCC827) have a significantly lower density (1.0416 ± 0.0006) than the cells with higher metastatic potential (H1975, 1.0491 ± 0.0021 g/mL). As a result, the passage time properties for the HCC827 and H1975 lines, when plotted versus cell volume, are similar (Fig. S8 *D* and *E*). Thus, differences between passage time properties for all three cell line pairs are consistent with expected deformability changes based on metastatic potential when accounting for buoyant mass, but not necessarily when accounting for volume. Changes in entry velocity and transit velocity in these three pairs of cancer cell lines are also compared based on the volume (Fig. S9). Similar to what we found with buoyant mass (Fig. 6), T_{Met} versus T_{nonMet} and H1975 versus HCC827 showed that a significant change in transit velocity was associated with the change in entry velocity (Fig. S9*A*). Furthermore, just as when accounting for cell buoyant mass, the proportional change in entry velocity relative to transit velocity was different among the three pairs when accounting for cell density (Fig. S9*B*). Therefore, differences in cell density did not alter the trends seen in entry and transit velocities.

SI Materials and Methods

Shear-Thinning Model. To check the quality of the cell trajectories observed in the suspended microchannel resonator (SMR), and also to make our results more readily comparable to those obtained via other assays of cell deformability, we compared the observed trajectory data to a classical biophysical model of cell entry into a constriction, the power law viscosity "shear-thinning" model (1). We chose the shear-thinning model because it is a relatively simple model (having only two parameters) that nevertheless has succeeded in capturing mechanical behavior in past experiments (1).

In the shear-thinning model, the cytoplasm is assumed to be a homogeneous fluid with a viscosity that depends on the shear rate of the material according to the following formula:

$$\mu(x,t) = \mu_0(\gamma(x,t)/\gamma_0)^{-b},$$

where $\gamma(x,t)$ is the shear rate at position x and time t, $\mu(x,t)$ is the viscosity at position x and time t, γ_0 is a reference or typical shear rate, μ_0 is a base viscosity, and b is a coefficient that determines how strongly the viscosity decreases with shear rate. Note that, although the model has three parameters (γ_0, μ_0, and b), γ_0 is not independent from the others and can be absorbed into μ_0; it is included only so that μ_0 has dimensions of a viscosity and can be interpreted as the viscosity at a specific shear rate. Thus, μ_0 and b are the key parameters of the model.

Model Computation. The following assumptions are made to apply the shear-thinning model to our measurement. First, to simplify the mathematics, we assume that the constriction has a circular cross-section, although its shape is rectangular. Under the shear-thinning model, the differences between entry into a rectangular constriction of the SMR and entry into a circular constriction of the same cross-section are small, and therefore, this is generally

a good approximation. Second, to decrease computation time, we make the approximation that the viscosity depends on the spatial average of the shear rate over the cell, rather than the local shear rate, so that $\mu(x,t) = \mu(t) = \mu_0 ([\gamma(x,t)]_x/\gamma_0)^{-b}$, where $[\gamma(x,t)]_x$ is the average shear rate over the volume of the cell at a given time. This approximation makes the model simulation more tractable and was also used by Tsai et al. (1).

With these simplifying assumptions, the entry of the cell into the constriction can be solved semianalytically. The position of the center of mass as a function of time reduces to the one-dimensional ordinary differential equation (ODE), as described in equations A3–A15 of ref. 1, which can easily be solved numerically. Because the entry times of the cells vary over several orders of magnitude, the ODE is solved with a variable time step, adaptively set so that the full cell entry consistently contains ~30 time steps. In addition, the final steps of cell entry is sampled more finely than the earlier steps because in the shear-thinning model the cell accelerates over time and most of the motion of the center of mass occurs near the end of the entry process.

Trajectory Preprocessing. Before being applied to the shear-thinning model, the cell trajectories are preprocessed by converting the resonant frequency to the position along the cantilever using the analytic method described by Dohn et al. (2). Next, because the sampling rate is not perfectly uniform in time (the sampling rate is proportional to the resonant frequency, which varies slightly by design of the cantilever), we use cubic spline interpolation to impose a uniform sampling rate of 2 kHz. A moving average filter is then applied to each cell's trajectory, with the length of the window equal to 5% of the cell's passage time. This filter is not applied to the very small number of initial samples in which the cell moves rapidly along the cantilever before reaching the constriction.

Alignment Procedure. The shear-thinning model accounts for only the cell entry into the constriction and makes no attempt to model cell behavior before it enters the constriction, as it is passing through the constriction, or after it exits the constriction. In fitting the observed entry times to the entry times predicted by the model, we need to identify where the entry begins and ends in the observed data. Here, we present data acquired by using a schematic alignment method, which uses the schematic layout of the SMR device to infer where along the cantilever the entry begins and ends. The entry is assumed to begin when the front tip of the cell reaches the entrance of the constriction, and to end when the back tip of the cell is first fully inside the constriction. One can alternately attempt to infer the entry region from the trajectory data itself, or to focus solely on the passage time. In practice, we found these different approaches to produce nearly identical results.

Fitting Procedure. As discussed above, the choice of γ_0 is arbitrary; we choose $\gamma_0 = p/4\mu_0$, where p is the pressure difference driving the cell through the constriction. Given this choice, we need to only fit b and μ_0. As described in the main text and Fig. 2, both a single-cell version and a population-level version of the model are used. In the population-level version, we assume that each cell has the same value of b and μ_0 (i.e., all cells are rheologically identical). The values of b and μ_0 are chosen to maximize the match between the observed and predicted entry times over all of the cells. The predicted entry time is calculated by the numerical procedure described in *Model Computation*, whereas the observed entry time is calculated by one of the three methods described in *Alignment Procedure*. Newton's method is used to iteratively select values of b and μ_0 such that the regression line of log(predicted entry times) versus log(observed entry times) has a slope of 1 and an offset of zero, i.e., predicted time matches observed time on average over the range of entry times and without any bias. Newton's method is initialized using $b = 0.5$ and μ_0 having a value appropriate to the average observed entry time, and terminated when the slope of the regression line converged to 1 ± 0.02. The method usually reaches the convergence in less than four iterations.

For the single-cell version of the model, we allowed each cell to have its own value of b, although we still fixed μ_0 at the population average determined from the population-level model. We chose the value of b for each cell that exactly matched the model's predicted entry time to the observed entry time, using Newton's method to iteratively select the correct value of b, again with 2% bounds on accuracy. We were then able to evaluate the quality of the model fit based on the detailed match between the observed and predicted trajectories (*Computation of Fitting Errors*), which was an independent measure because, aside from the endpoints, it was not used to fit the model.

In addition to the parameters μ_0 and b, we also incorporated an optional parameter into the single-cell version of the model, namely an initial projection into the constriction. The initial projection means that, at the initial entry, the cell is assumed to already have a small volume inside the constriction, so that the entry curve is slightly shifted upward. In previous studies, as well as in our current data (Fig. S2), this slight shift can greatly improve the match between the model and the observed data. The purpose of the initial projection was to account for a brief period of initial rapid elastic entry into the constriction at the beginning of the entry phase. This addition was required to make the original shear-thinning model described by Tsai et al. (1) to work.

Computation of Fitting Errors. The quality of the model fit is evaluated, particularly in the single-cell model, using a metric that compares the model's predicted trajectory and the trajectory observed in the SMR device. We interpolated both the predicted and observed trajectories to the same 100 evenly spaced time points using a cubic spline interpolant, and then computed the root mean square difference between the predicted and observed trajectories. Because the spatial distance between the beginning and end of cell entry differs from cell to cell due to differences in cell buoyant mass, the model fit score is normalized by this spatial distance. The overall score is thus given by the following:

$$\text{Model Error Score} = \frac{1}{[x(t_N) - x(t_0)]} \sqrt{\frac{1}{N} \sum_{i=0}^{N} (x(t_i) - y(t_i))^2},$$

where $x(t_i)$ is the observed cell position at time point t_i, $y(t_i)$ is the model-predicted cell position at time point t_i, and N is the number of time points. The error score is 0 for a perfect match and 1 for the worst possible match between any two curves from $x(t_0)$ to $x(t_N)$.

Data Processing. To obtain buoyant mass and passage time information from the acquired resonant frequency data, each peak was smoothed using a Savitzky–Golay filter and fit to a fourth-order polynomial at the peak tip. The peak height is proportional to the buoyant mass of the cell. Because the resonant frequency also depends on the position of the cell in the cantilever (2), and the position of the constriction within the cantilever is known, the passage time of the cell is thus taken to be the time from the start of the entry to the exit of the constriction. Entry and transit velocities are extracted from the acquired data by converting the resonant frequency to the normalized position of the cell in the cantilever, and then taking the time derivative of the normalized position. We define entry velocity as the minimum velocity of the cell as its center of mass approaches the constriction from ~10 μm away. Then we define transit velocity as the velocity of the cell where its center of mass reaches ~10 μm inside of the constriction. Extracting velocities at those positions enables reliable comparisons of velocities between cell lines. To estimate the

velocity differences between cell lines or after a given treatment, two sets of velocity data in log–log scale from each condition were fitted to linear models with a fixed slope and variable intercepts corresponding to the two conditions (Fig. S12). The difference between the two intercepts is log of the ratio, which is then converted to the actual ratio.

Density Measurements. Buoyant mass is defined by the product of the cell's volume and its density difference from the surrounding fluid. The density of a cell from a given sample can be estimated by using the SMR and a Coulter counter (Multisizer 4; Beckman Coulter) to measure the buoyant mass and volume, respectively, of cells from the same sample (3). In brief, cells were cultured under standard conditions, and samples were prepared by resuspending the cells in RPMI 1640 medium [prepared by dissolving 16.2 g of RPMI 1640, 2 g of $NaHCO_3$, 10% (vol/vol) FBS, 100 IU of penicillin, and 100 μg/mL streptomycin in water for a final volume of 1 L at pH 7.2]. The samples were then loaded in the SMR and the Coulter counter. Histograms were made from buoyant mass (n = ~300–600) and volume measurements (n = ~5,000–10,000), which were then fitted to log-normal functions to find the mean values of buoyant mass and volume for the measured cells. The density of the cell population is given by $\rho = \rho_f + m_B/V$, where ρ is the cell density, ρ_f is the fluid density, m_B is the buoyant mass, and V is the cell volume. Means from fitting buoyant mass and volume data were substituted into m_B and V, respectively. Also, the density of the fluid, ρ_f, was found by calibrating the SMR with solutions of known density. Measurements were repeated three to four times for each cell line from cultures of varying passage number. The average cell density calculated from replicate experiments was used to convert the existing buoyant mass data (Figs. 3 and 6) to volume. With these calculations, the passage time, entry velocity, and transit velocity data are compared again based on cell volume.

1. Tsai MA, Frank RS, Waugh RE (1993) Passive mechanical behavior of human neutrophils: Power-law fluid. *Biophys J* 65(5):2078–2088.
2. Dohn S, Svendsen W, Boisen A, Hansen O (2007) Mass and position determination of attached particles on cantilever based mass sensors. *Rev Sci Instrum* 78(10):103303.
3. Bryan AK, Goranov A, Amon A, Manalis SR (2010) Measurement of mass, density, and volume during the cell cycle of yeast. *Proc Natl Acad Sci USA* 107(3):999–1004.

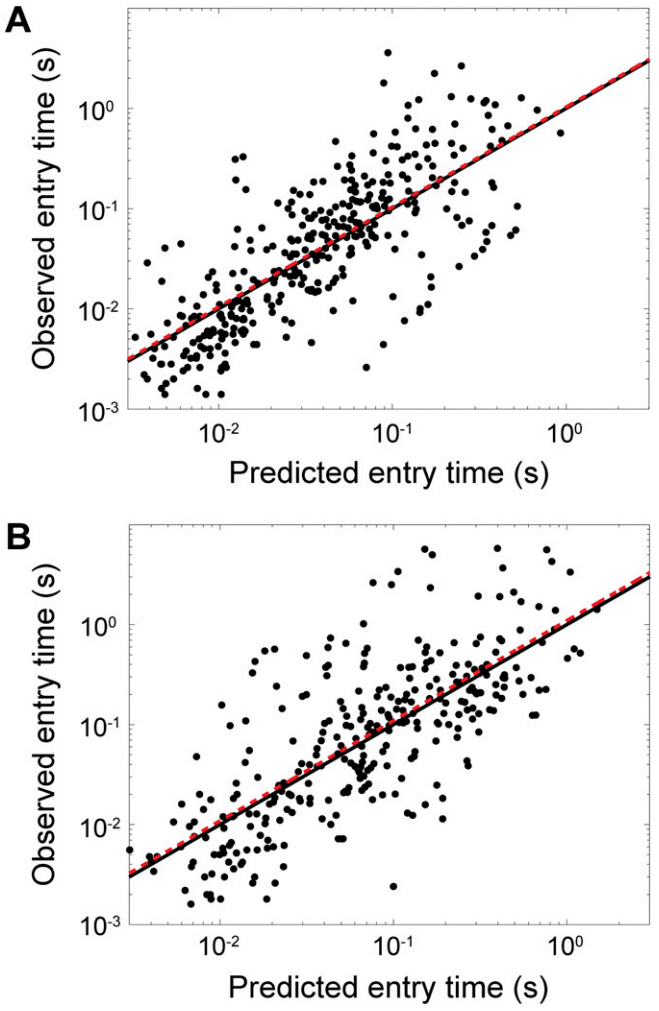

Fig. S1. Entry times observed in the SMR can be predicted with high accuracy from a power law viscosity model. Cells are modeled as having a shear rate-dependent viscosity $\mu = \mu_0(\gamma)^{-b}$, where a single best-fit b and μ_0 are chosen for a training set of cells and then applied to a test set. The black dots are measurements for individual test cells. The dashed red line is the regression line for the test cells. The black line shows equality between predicted and observed times. (*A*) Prediction of entry times for H1975 cells (n = 343) gives a correlation coefficient of r = 0.73 for the training set and 0.76 for the test set. (*B*) Prediction of entry times for HCC827 cells (n = 318) gives a correlation coefficient of r = 0.74 for the training set and 0.74 for the test set.

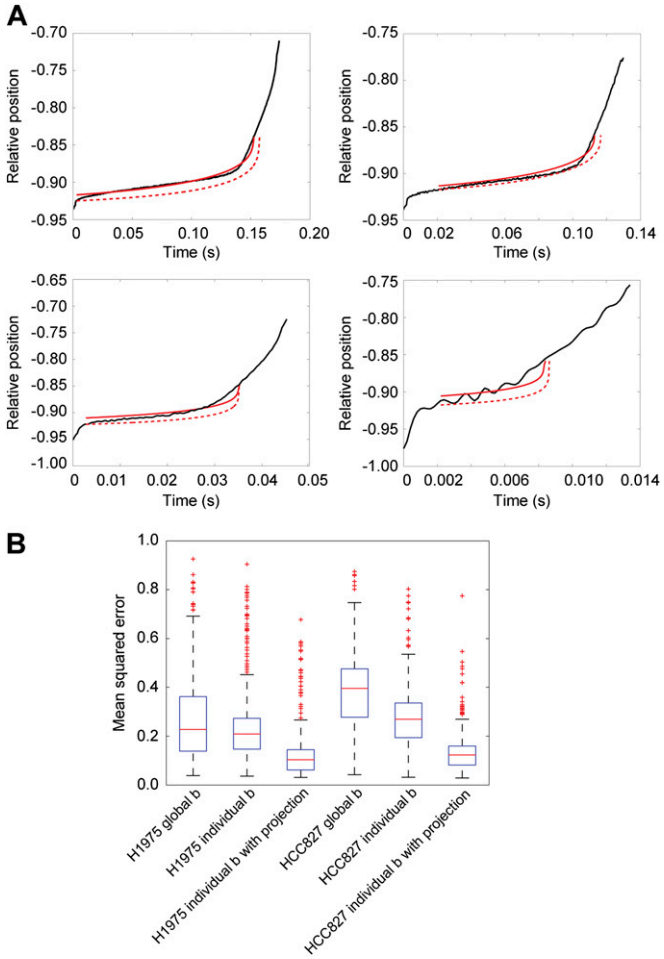

Fig. S2. The fit between power law viscosity model and cell trajectories measured in the SMR. (*A*) Empirical trajectory of H1975 (black) is fit to the model with (solid red) and without (dotted red) an initial projection. The best (*Upper Left*), 75th percentile (*Upper Right*), median (*Lower Left*), and 25th percentile (*Lower Right*) quality fits are shown. (*B*) Box-and-whiskers plot of the fit quality for H1975 and HCC827 cells using different fit approaches; best population b, best b per cell, and best b per cell with projection.

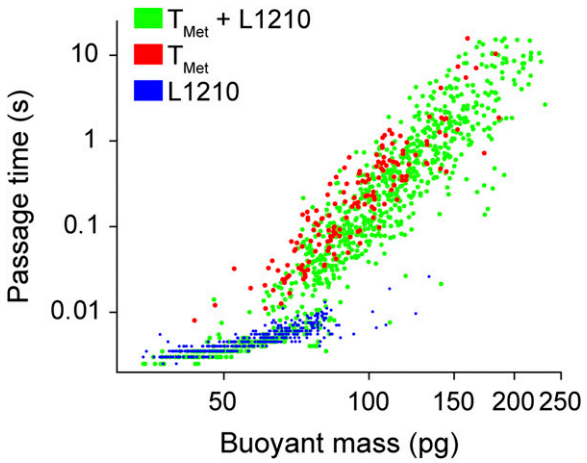

Fig. S3. Passage time versus buoyant mass for T_{Met} and L1210 cell lines. T_{Met} (red, $n = 160$), L1210 (blue, $n = 405$), and a mixture of T_{Met} and L1210 (green, $n = 892$) were measured under the same conditions. Mouse lung cancer cells (T_{Met}) require more time to pass through the constriction than mouse blood cells (L1210) of similar buoyant mass. Measurements were acquired with a PEG-coated channel surface and using a pressure drop of 0.6 psi.

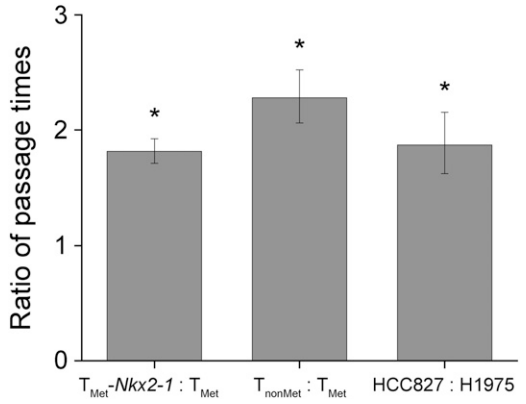

Fig. S4. The ratio of passage times in Fig. 3 *D–F*. Two sets of passage times in log–log scale from each cell line were fit to a linear model in which both conditions were constrained to have the same slope, but were allowed different intercepts via a differential intercept term, which provides a vertical offset for one condition relative to the other (Fig. S12). This differential term can be interpreted as the log of the ratio of the two sets of passage times, controlling for the effects of varying buoyant masses. The ratios of passage times for each pair obtained from these models are plotted. To determine whether cell lines exhibited statistically different passage times when controlling for the effects of buoyant mass, we applied a *t* test to the differential intercept term in our model. In all three pairs in Fig. 3 *D–F*, the differences in intercepts were significant ($*P < 2 \times 10^{-16}$ for all three pairs). Error bars represent 95% confidence intervals.

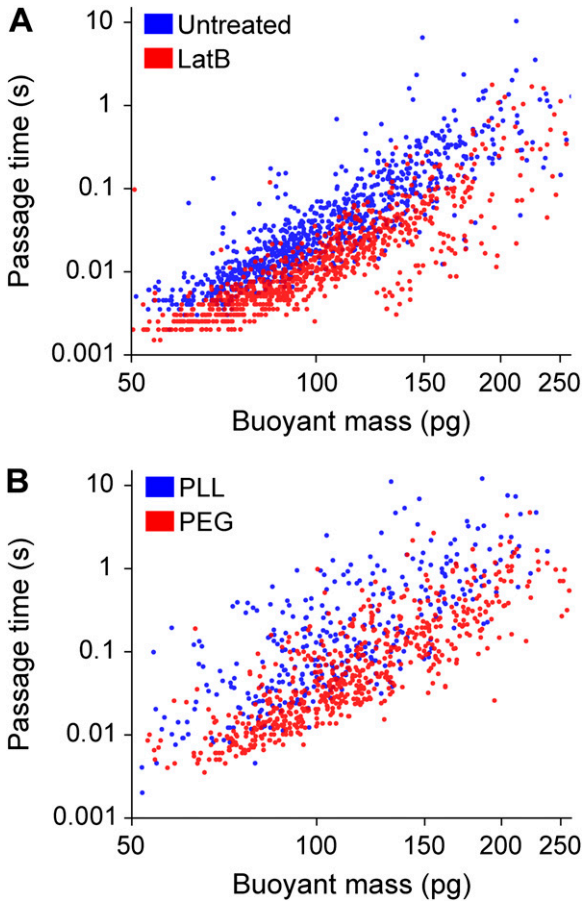

Fig. S5. Changes in the passage time of H1975 cells after perturbing either deformability or microchannel surface charges. The data match with those of Fig. 5. (*A*) Passage time versus buoyant mass for H1975 untreated (blue) and treated with latrunculin B (LatB) (red). Treatment with LatB decreases the passage time. (*B*) Passage time versus buoyant mass for H1975 for a microchannel surface coated with positively charged poly-L-lysine (PLL) (blue) and neutral PEG (red). Coating with PLL increases the passage time.

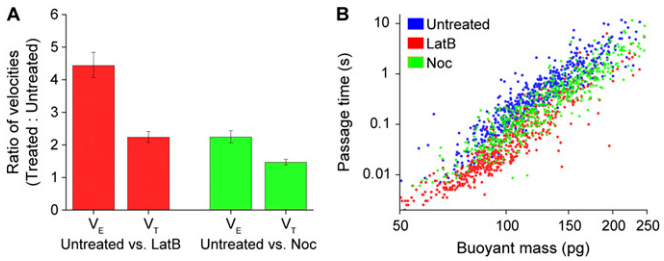

Fig. S6. Effects of latrunculin B (LatB) (5 μg/mL, 30 min) and nocodazole (Noc) (1 μg/mL, 30 min) were tested with MEF cells and compared with untreated control. (*A*) Treating with LatB (red bars) and Noc (green bars) both resulted in a relatively larger increase in the entry velocity than the transit velocity but LatB induced greater change than Noc. Error bars represent 95% confidence intervals. (*B*) LatB and Noc both induced a decrease in the passage time but the extent of the change was greater with LatB (untreated, blue, $n = 570$; LatB, red, $n = 494$; Noc, green, $n = 534$). Measurements were acquired with a PEG-coated channel surface and using a pressure drop of 1.35 psi.

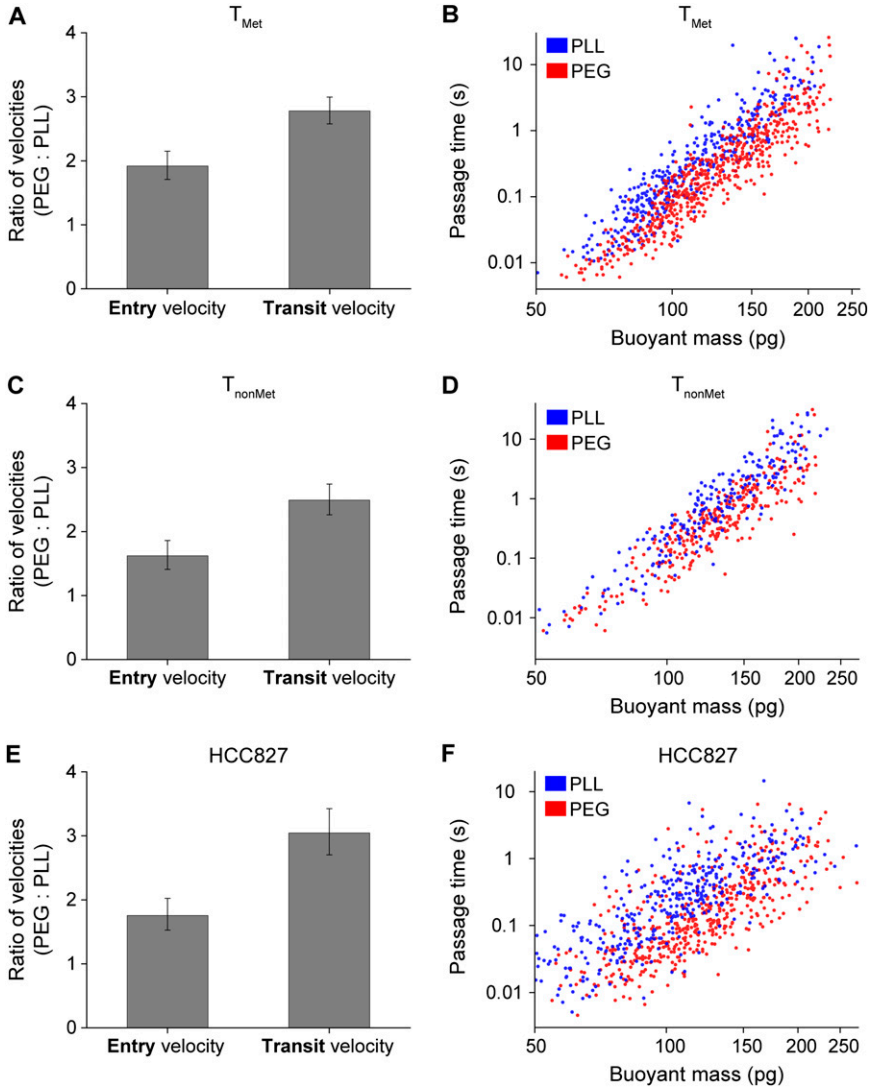

Fig. S7. Effect of PEG versus PLL surfaces was tested with various cell lines: T_{Met} (*A* and *B*; $n = 396$ for PLL, $n = 572$ for PEG), T_{nonMet} (*C* and *D*; $n = 220$ for PLL, $n = 320$ for PEG), and HCC827 (*E* and *F*; $n = 403$ for PLL, $n = 488$ for PEG). For all three cell lines, PLL-coated microchannel induced a greater change in the transit velocity than the entry velocity (*A*, *C*, and *E*) as well as an increase in the passage time (*B*, *D*, and *F*). The distinct changes in entry and transit velocities caused by PEG versus PLL surfaces were consistent with those observed with H1975 cells (Fig. 5). Error bars represent 95% confidence intervals. Measurements were acquired using a pressure drop of 0.9 psi for the mouse cell lines (T_{Met}, T_{nonMet}) and 1.8 psi for the human cell line (HCC827).

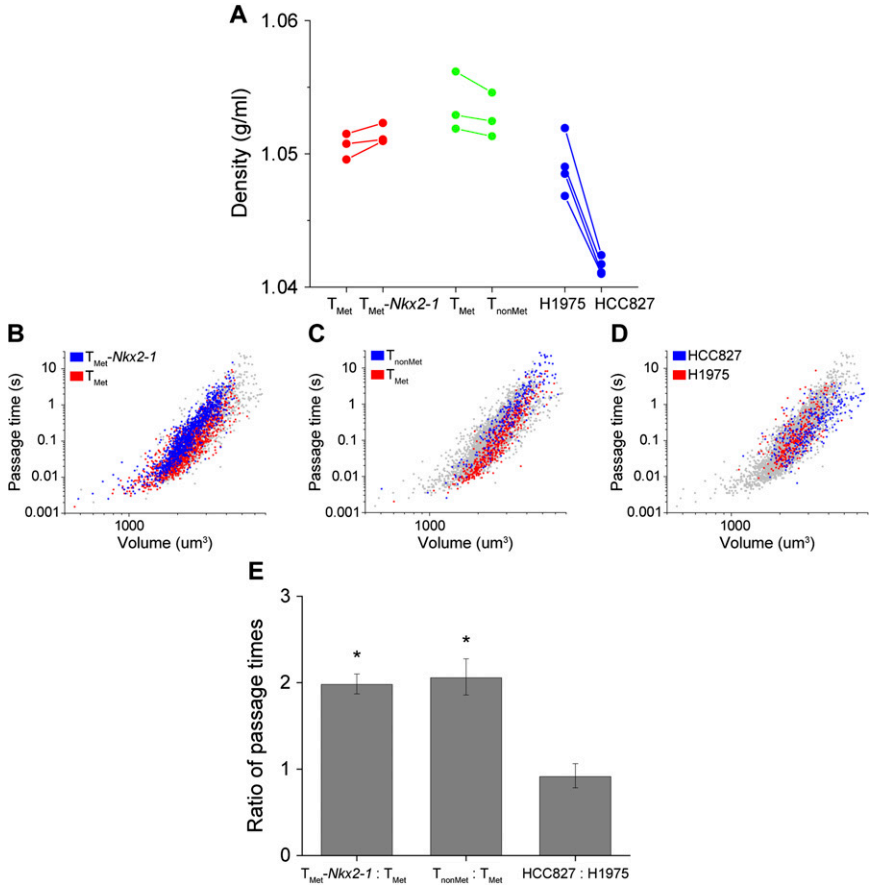

Fig. S8. Passage times of cancer cells with varying metastatic potentials (Fig. 3 *D–F*) are compared based on cell volume. (*A*) Density measurements of three pairs of cancer cell lines. T_{Met} versus T_{Met}-*Nkx2-1*, T_{Met} versus T_{nonMet}, and H1975 versus HCC827 were repeated from different cultures three, three, and four times, respectively. Each measurement is connected by a line. Then, cell buoyant mass was converted to volume by using the average density of each cell line. The passage time versus cell volume is plotted for (*B*) T_{Met}-*Nkx2-1* (blue), T_{Met} (red), (*C*) T_{nonMet} (blue), T_{Met} (red), (*D*) HCC827 (blue), and H1975 (red), using the same data set as in Fig. 3 *D–F*. The gray dots shown as a background correspond to the collection of cell lines. (*E*) The difference in passage times based on the cell volume shown in *B–D* is estimated as the ratio using the same method described in Fig. S4. The difference in T_{Met} versus T_{Met}-*Nkx2-1* and T_{Met} versus T_{nonMet} remained significant ($*P < 2 \times 10^{-16}$). However, the difference in H1975 versus HCC827 was not significant ($P = 0.246$). Error bars represent 95% confidence intervals.

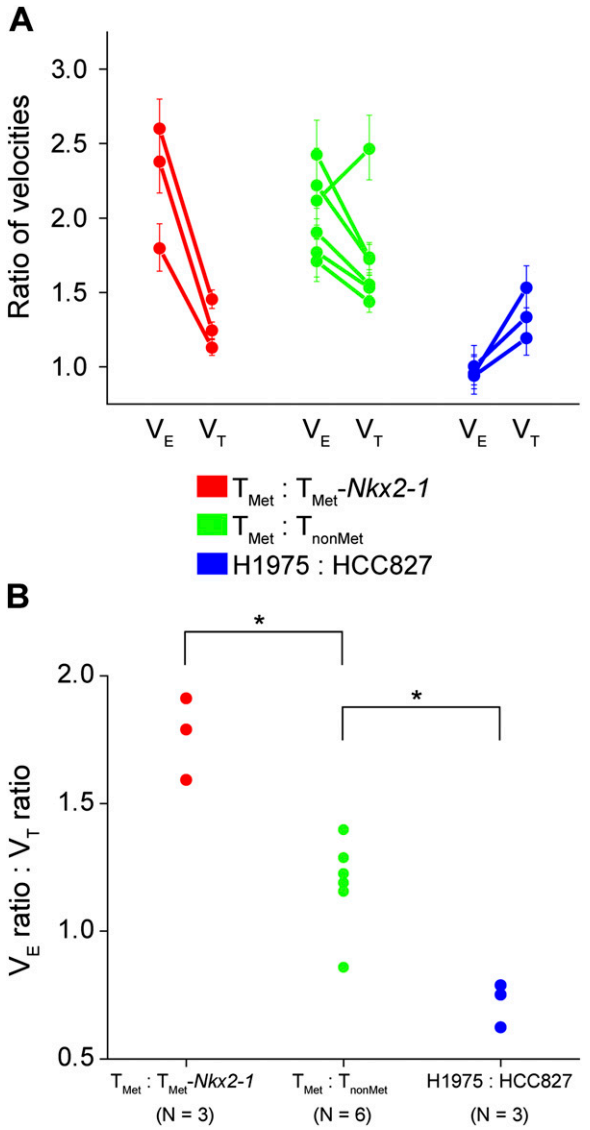

Fig. S9. Changes in entry velocity (V_E) and transit velocity (V_T) in three pairs of cancer cell lines shown in Fig. 6 are compared again based on the volume. The buoyant mass is converted to the volume using the average density as shown in Fig. S8. (*A*) Ratio of V_E and ratio of V_T based on the cell volume. Similar to Fig. 6*A*, T_{Met} versus T_{nonMet} and H1975 versus HCC827 showed that a significant change in transit velocity was associated with the change in entry velocity. Error bars represent 95% confidence intervals. (*B*) The ratio of V_E divided by the ratio of V_T based on the cell volume. Similar to Fig. 6*B*, the proportional change in V_E relative to V_T was different among the three pairs. A Mann–Whitney–Wilcoxon test showed significant differences ($*P < 0.05$) between T_{Met} versus T_{Met}-*Nkx2-1* and T_{Met} versus T_{nonMet} ($P = 0.0238$), and between T_{Met} versus T_{nonMet} and H1975 versus HCC827 ($P = 0.0238$).

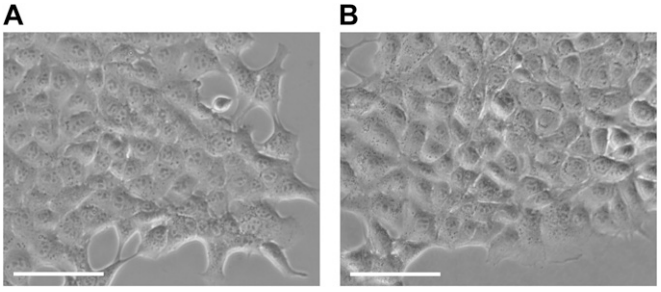

Fig. S10. After having been measured in the SMR device, cells remained viable and proliferated well, having similar morphology as unprocessed control cells. Phase contrast images of the control cells (*A*) and the cells measured in the device (*B*). T_{Met} cells grown under the standard condition were harvested. One-half of the sample was kept in the 37 °C incubator as an unprocessed control sample, whereas the other half was measured in the SMR for 30 min and collected. At the end of experiment, the viability of the control and SMR-measured cells assayed by trypan blue were 96% and 94%, respectively. The two samples were separately transferred to 12-well plates with a similar seeding density. Images were taken 3 d after the seeding. (Scale bar, 100 μm.)

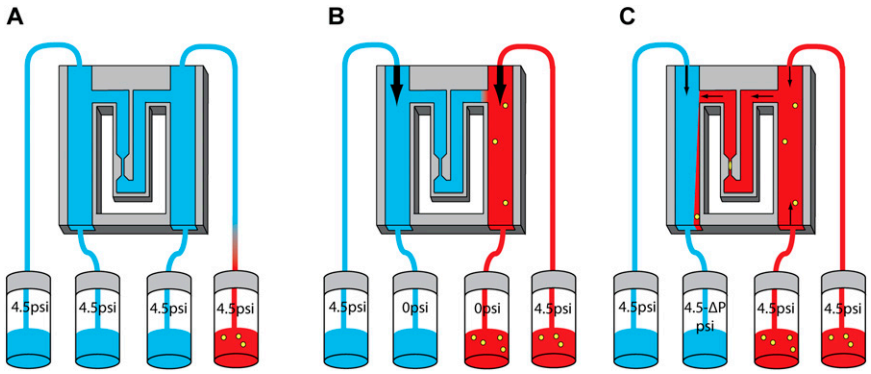

Fig. S11. Diagram of measurement system. (*A*) The system consists of two parallel fluidic paths (bypass channels) that are connected through the SMR device. Before the cells are loaded, the system is filled with cell culture medium (blue). Cell solution is introduced from one upstream vial (red), whereas the other three vials are filled with medium. The upstream vial with cell solution is kept at 37 °C. Fluid flow through the four fluidic access ports, which are connected to two upstream and two downstream vials, is controlled by pressure regulators. A constant pressure drop is created across the fluidic channels by the pressure regulators to send the cells through the SMR for the measurements. (*B*) To start loading a cell solution, lower pressure is applied to two downstream vials, and, as a result, one of the bypass channels is filled with the cell solution. (*C*) Fluid flow through the SMR is created by applying lower pressure only at one downstream vial, which collects cells exiting from the SMR, while the other three vials maintain matched pressures.

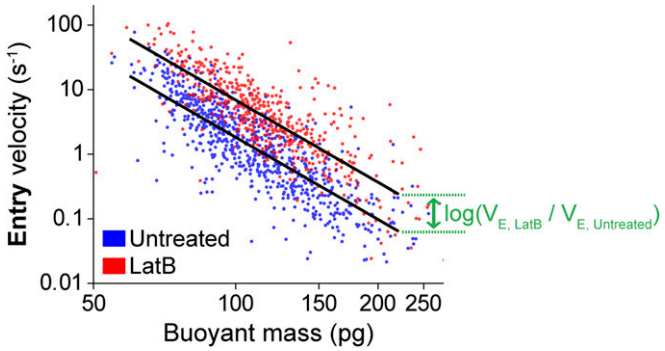

Fig. S12. The dataset from Fig. 5*A* is shown as an example of calculating the ratio of velocities. The difference in the entry velocity between untreated (blue) and LatB-treated (red) H1975 cells is quantified by the ratio. Because the entry velocity strongly depends on the power law relationship, the two datasets, i.e., untreated and LatB-treated, in log–log scale are fitted to the linear models (black lines) with a fixed slope and variable intercepts corresponding to the two conditions. The difference between the two intercepts (green arrow) is log of the ratio, which is then converted to the actual ratio.

Table S1. List of materials for each cell line

Cell lines	Culture media	Dissociation
H1975 HCC827 H1650	RPMI (Invitrogen) supplemented with 10% FBS (Invitrogen), 1% sodium pyruvate (Invitrogen), 100 IU of penicillin, and 100 μg/mL streptomycin (Invitrogen)	TrypLE (Invitrogen)
T_{Met} T_{nonMet} T_{Met}-*Nkx2-1*	DMEM (Cellgro) supplemented with 4.5 g/L glucose, 10% FBS (Gibco), 1% L-glutamine (Gibco), 100 IU of penicillin, and 100 μg/mL streptomycin (Cellgro)	0.25% Trypsin/2.21 mM EDTA (Cellgro)
MEF (immortalized)	DMEM (Cellgro) supplemented with 4.5 g/L glucose, 10% FBS (Thermo Scientific), 100 IU of penicillin, and 100 μg/mL streptomycin (Sigma-Aldrich)	0.25% Trypsin/2.21 mM EDTA (Cellgro)
L1210	L15 (Invitrogen) supplemented with 1 g/L glucose (Sigma-Aldrich), 10% FBS (Invitrogen), 100 IU of penicillin, and 100 μg/mL streptomycin (Gemini)	Grown in suspension